Received: 4 May 2020 | Revised: 12 August 2021 | Accepted: 13 August 2021

DOI: 10.1002/esp.5237

RESEARCH ARTICLE

ESPL WILEY

Size–frequency distribution of shallow landslides in the Black Forest, Germany

Matthias Büschelberger | Jakob Wilk | Stefan Hergarten | Frank Preusser

Institut für Geo- und Umweltnaturwissenschaften, Albert-Ludwigs-Universität Freiburg, Albertstrasse 4 5 23b, 79100 Freiburg i. Br., Germany

Correspondence
Jakob Wilk, Institut für Geo- und Umweltnaturwissenschaften, Albert-Ludwigs-Universität Freiburg, Albertstrasse 4 5 23b, 79100 Freiburg i. Br., Germany.
Email: jakob.wilk@geologie.uni-freiburg.de

Summary

Landslides are a major hazard in mountainous regions, represent a threat to human life, and cause substantial economic costs. While some landslide hazard assessments, including hazards maps, are available for Germany, their spatial coverage is not uniform. In the Black Forest, several landslides have recently attracted public attention, but the landslide hazard in this region has received limited consideration in literature to date. This study focuses on the spatial pattern and size distribution of soil-borne landslides in the submountainous valley of Menzenschwand. A combination of remote sensing, geophysical surveying, and geotechnical testing was used to map and characterize the landslide inventory of two selected hillslopes. In the statistical analyses, we observe a larger proportion of small-scale landslides with size below 100 m^2 than usually reported in similar studies. This effect may be related to the low cohesion of the soil (glacial deposits). As a major result, a cutoff in the distribution at large landslide sizes compared with the expected power-law tail of the distribution was found. While the maximum landslide size found in this study was about 1100 m^2, the largest landslide should theoretically be at least 2500 m^2 at 95% probability. The cutoff at large sizes is probably due to the limited soil thickness, where about 50% of the considered area has a depth to bedrock of 1 m or less. For the considered location, this result suggests that an increase in frequency and intensity of rainstorms should predominantly result in an increase of landslide frequency, but without increasing the size of the largest landslides. As a more general implication, the contribution of large landslides to the total hazard may be overestimated if soil thickness is not considered, in particular if the present-day hazard is projected to future scenarios.

KEYWORDS
landslide hazard, Pareto distribution, digital surface models, GPR survey, geotechnical analysis, remote sensing, soil-borne landslides, drone photogrammetry, near-surface geophysics

1 | INTRODUCTION

The frequency and size of landslides in mountainous areas and the related risk to human life and infrastructure are potentially affected by climate change (e.g., Crozier, 2010; Gariano & Guzzetti, 2016), except for those triggered by earthquakes (e.g., Keefer, 1994; Meunier et al., 2007). This applies to landslides involving bedrock in high mountains due to the retreat of permafrost as well as to landslides in unconsolidated sediments (i.e., soils in a geotechnical sense). The latter occur in almost all mountain ranges and are often triggered by rainstorms or rapid snow melt, so that a change of landslide hazard can be expected if precipitation and temperature patterns change in the future. Shallow landslides, being bound to these mechanisms (Crosta, 1997), are used synonymous with soil-borne landslides in this text.

Since landslides represent a threat to humans life and their economic costs are substantial (Klose et al., 2014), increasing efforts have been made to assess landslide hazards on both global and regional

scales (e.g., Chacón et al., 2006). The ultimate goal is to produce maps showing the spatial incidence of landslides, reveal their spatiotemporal incidence and forecast their occurrence, as well their potential consequences. Although landslides cause damage totaling about US $300 million in Germany annually (Klose et al., 2015), knowledge about their impact is still based on limited data. In particular, the spatial coverage of such information is not uniform, with a main focus on areas such as the uplands of central Germany (e.g., Damm et al., 2009, 2010), the Swabian Alb (e.g., Bell et al., 2006; Neuhäuser & Terhorst, 2007), and the Alps including their foreland (e.g., Nie et al., 2017). Damm and Klose (2015) introduced a national landslide database for Germany, although still with limited and nonuniform spatial coverage. In total, at least 23 national landslide databases exist in Europe (Damm & Klose, 2015).

The statistical distribution of event sizes has become a central part of hazard assessment. Pareto distributions, also called power-law distributions, are now frequently used in the assessment of major geohazards (e.g., Stark & Hovius, 2001). Whenever a certain type of hazard is characterized by a universal size distribution, i.e., by a distribution that is independent of the triggering mechanism and site-dependent conditions, an extrapolation of the hazard to event sizes lying outside the range of the inventory available at a given location becomes possible. This is particularly helpful if the available inventories are either restricted to a small domain or cover only a short time span. Thus, although the statistics of large events are often insufficient, their expected frequency can be estimated from the larger number of smaller events contained in an inventory. For Pareto-distributed hazards, however, attention must be paid to the tail of the distribution. Practically, Pareto distributions break down at very large event sizes, and this breakdown or the transition to another type of distribution is particularly relevant in the context of risk (Hergarten, 2004).

Earthquakes were the first (Gutenberg & Richter, 1954) and are still the most widely studied example in this context. Interest in power-law distributions rapidly increased after the theoretical concept of self-organized criticality was introduced (Bak et al., 1987; Bak, 1996; Hergarten, 2002; Jensen, 1998). The power-law distribution of wildfires was even predicted by a simple model (Drossel & Schwabl, 1992) several years before it was recognized in real data (Malamud et al., 1998). Nowadays, this has become an essential part of the discussion about the impact of climate change on wildfire hazard, and simple models have turned out to be able to explain some effects, for example, the statistical difference between natural and human-induced fires (Krenn & Hergarten, 2009).

The first study where a power-law distribution of landslide sizes was found is more than 50 years old (Fuyii, 1969). However, it took almost 20 years for this topic to become popular through comprehensive studies mapping several thousand landslides (Hovius et al., 1997) and modeling approaches (Densmore et al., 1998; Hergarten & Neugebauer, 1998) attempting to bring landslides into the context of self-organized criticality. The power-law size distribution of landslides turned out to be more complicated than those of earthquakes and wildfires. First, there seem to be two distinct groups of landslides. Both landslides in non-consolidated layers and those involving bedrock follow power-law distributions over some range, but with strongly different exponents. In turn, the differences within each class seem to be small, and the distribution was found to be independent of the triggering mechanism (e.g., earthquakes, rainstorms, or rapid snow melt). These results were obtained by Malamud et al. (2004) from a few inventories and confirmed by Brunetti et al. (2009) when comparing a larger number of datasets.

Second, the size distribution of landslides in soil shows a strong deficit at small sizes compared with the theoretical Pareto distribution. This deficit has been attributed to incompleteness of the inventories by Stark and Hovius (2001), while Malamud et al. (2004) considered it to be a real property. As cohesion stabilizes slopes at small scales but becomes less important for large slope failures, a deficit of small landslides can in principle be explained by soil mechanics. However, recent work (Li et al., 2014; Tanyas et al., 2018) showed that there is still no full consensus about the origin of the deficit of small events in landslide inventories. The same holds for the origin of the power-law tail at large landslide sizes. Although some new modeling approaches have been presented in recent years (Alvioli et al., 2014; Frattini & Crosta, 2013; Jeandet et al., 2019; Liucci et al., 2017), there still seems to be no unique and widely accepted explanation. For further insights into the scaling properties of landslides, the overview by Tebbens (2020) is recommended.

This study addresses landslide occurrence and the related hazard in the Valley of Menzenschwand in the Black Forest, a mountain range in the southwestern part of Germany (Figure 1). While a series of smaller and moderate events in recent years have attracted attention from the public and local authorities, to the best of the authors' knowledge, no related studies have been published in international literature to date. The study area (47°84′ N, 8°06′ E) is situated close to the community of Menzenschwand (which initialized this study), at about 900 m a.s.l. and southeast of the summit of Feldberg (1493 m a.s.l.), the highest peak in the Black Forest. The bedrock is mainly of intrusive origin (Bärhalde-granite, GB), followed to the east by metamorphic units of paragneissic composition (pgA and pg) (Wimmenauer & Schreiner, 1981). The crystalline rocks were formed during the Variscan orogeny of the Paleozoic and were uplifted again in the context of the formation of the Upper Rhine Graben during the Cenozoic (Pflug, 1982). During Pleistocene glaciations, the valley of Menzenschwand was excavated by the Alb glacier system (Geyer & Gwinner, 2011). Evidence of these glaciations are U-shaped valleys as well as cirques (Zienert & Fezer, 1967). The last glaciation also formed terminal moraines (Rahm, 1970) such as the Kluse moraines (We in Figure 1) north of the Menzenschwand waterfalls (Hantke & Rahm, 1976). Associated with the melting of the ice is the deposition of a glacial debris sheet (Wm), which widely covers the resident hillslopes and is mainly interpreted as till. Wimmenauer and Schreiner (1981) estimated the till to be only a few meters thick upon the polished bedrock. According to the same source, the filling of the valley is composed of fluvial and glaciofluvial sediments with a maximum thickness of about 45 m. Hence, our findings are restricted to regions with impermeable rock covered by unconsolidated deposits.

While the mean monthly precipitation at Menzenschwand is about 150 mm, maximum values of more than 300 mm occur during winter (Figure 2). Outstanding peaks of more than 500 mm occurred in December 2011 and in January 2018. In contrast to typical winter maxima, the January 2018 event was accompanied by moderate formation of fresh snow. A considerable amount of precipitation was contributed by a rainstorm that initiated some of the landslides investigated in this study.

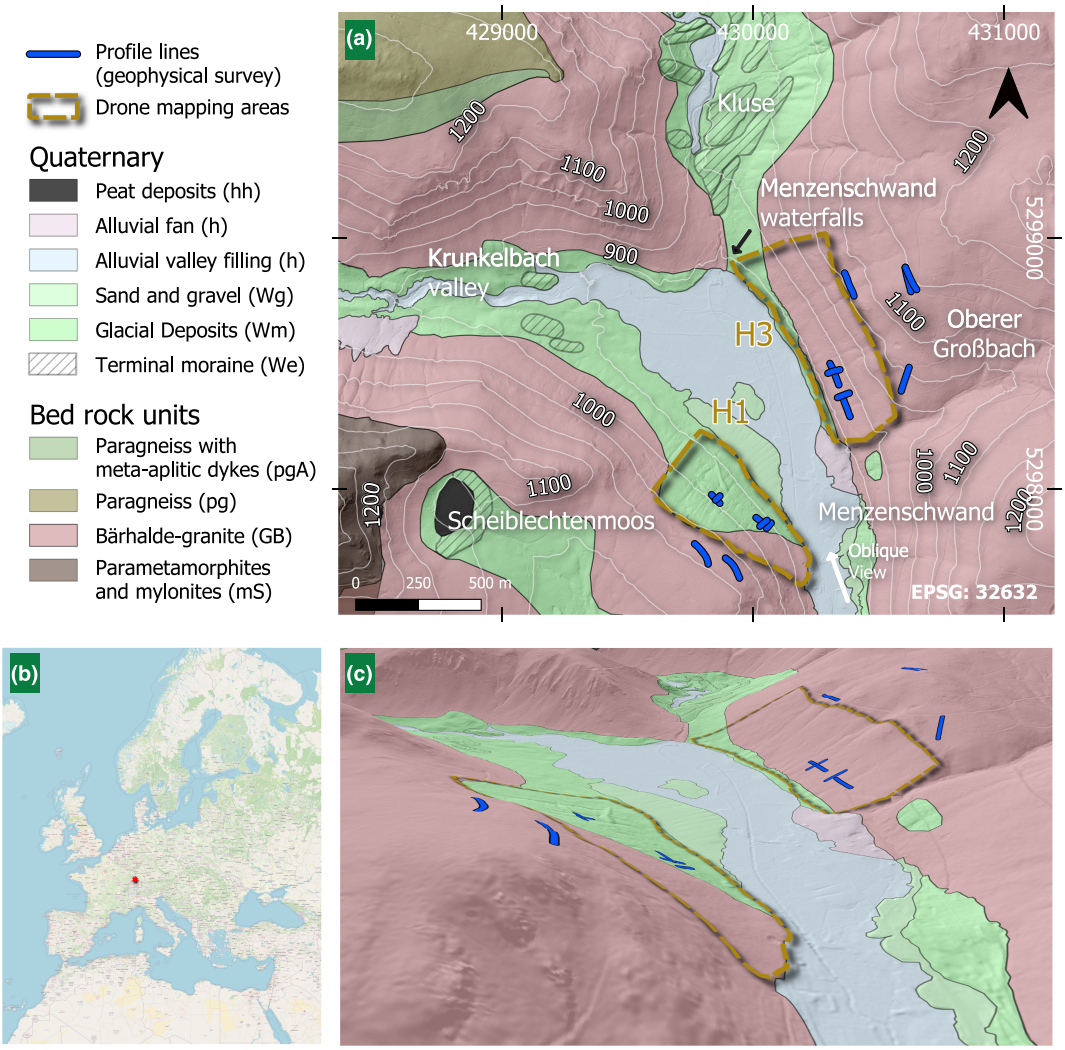

FIGURE 1 Overview of the study area. (A) Geological map of Menzenschwand with the boundaries of hillslopes H1 and H3 as well as profile lines of the ground-penetrating radar survey. Geological units digitized after Wimmenauer and Schreiner (1981). (B) Location in Europe. (C) Oblique view with texture of the geological units from (A). Topography not exaggerated [Color figure can be viewed at wileyonlinelibrary.com]

FIGURE 2 Monthly precipitation data in the Menzenschwand area (DWD, 2019) [Color figure can be viewed at wileyonlinelibrary.com]

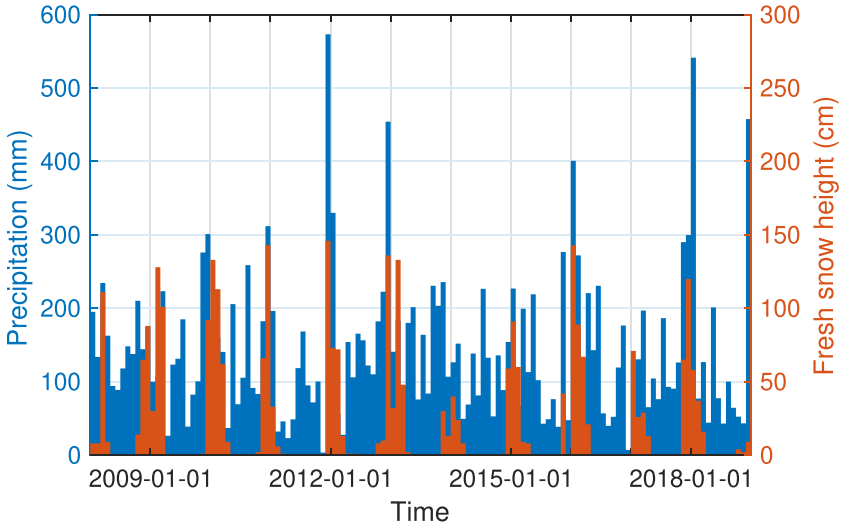

The particular situation with steep slopes where the bedrock is covered by a presumably thin layer of unconsolidated deposits raises several questions. The first is (i) whether or not the landslide sizes follow the typical distribution for soil-covered slopes discussed above. So far, only moderately sized landslides have been observed at Menzenschwand, but with high overall landslide frequency. However, for practical hazard assessment, the size of the largest landslides to be expected is particularly relevant. This leads to the next question of

(ii) whether landslides that cause serious damage to infrastructure or even threaten human life could also take place. This question is particularly relevant in the context of changing climatic conditions, e.g., in case the contribution of rainfall to winter precipitation increases. This study combines digital elevation models (DEMs) derived from photogrammetry in addition to light detection and ranging (LiDAR) data as well as near-surface geophysics and laboratory soil tests to provide a comprehensive overview of the spatial pattern of landslides and their statistical distribution in the Menzenschwand area. With regard to the specific geological setting, i.e., impermeable bedrock covered by thin layers of unconsolidated deposits, such as glacial sediments or regosols, this study could have implications for similar regions, beyond the scope of regional hazard assessment.

2 | FIELDWORK AND DATA ACQUISITION

2.1 | Landslide mapping

Recent and historical landslides were mapped on two slopes of the valley in September and October 2018. The southeastern slope has an extension of about 0.17 km^2 and is labeled H1 in Figure 1, while the northwestern slope is 0.24 km^2 in size and is labeled H3. Surface morphologies and current land use are similar within H1 and H3

Two separate flight plans (one for each hillslope) for a DJI Mavic Pro drone were generated using the Android app DroneDeploy v2.81.0. By default, sampling rates and paths were computed using the software's internal methods. The frontal and side overlap were kept constantly at 75% and 65% at a cruising altitude of about 110 m above the launch location, which was arranged at medium slope elevations of about 950 m a.s.l. This resulted in the construction of 216 camera views on H1 and 320 camera views on H3. By the use of a high-performance desktop computer, a local build of Agisoft Metashape Professional v1.5.2 was chosen for mesh and surface model generation. The depth reconstruction for each aligned camera led to the formation of point clouds representing H1 with about 230,000 data points and H3 with about 2.4 million data points. The following triangulation step produced a three-dimensional mesh with approximately 700,000 faces on H1, whereas H3 could be digitized with roughly 1.4 million faces. From this model, GIS-compatible Geotiffs were derived with pixel resolution of $\lesssim$10 cm for both slopes. The orthophotos with spatial resolution of $\lesssim$5 cm were delivered by texturing the cloud from a weighted-average mosaic (see Agisoft LLC, 2018, for further technical details).

As usually applied in drone photogrammetry, ground control points (GCPs) are key control features to ensure the accuracy of the resulting point clouds and elevation models with respect to real-world objects and their absolute coordinates. Since this study was carried out due to the interest from a small community (Village of Menzenschwand, population 500 people), the lack of financial resources meant that we had to discard the option of investing in borrowing high-precision continuous global positioning system (CGPS) units. The drone itself provided absolute georeferencing in terms of three-dimensional (3D) coordinates, whose precision is far more uncertain than those obtained using more dedicated devices. The root-mean-square (RMS) reprojection error of the point cloud has a reasonably low target value of 1.4 pixels. Of course, this parameter cannot be transferred to the uncertainty of the digital surface model. Nevertheless, combined with the fact that the raw data were obtained from a multi-perspective scan via DroneDeploy, it can be assumed that the relative axis distortion of the projected model is close to reality. This surely will not affect the absolute georeferencing of the data, but since only the relative sizes of mapped objects from the model (volume, scar surface area) are of interest, this will not affect the quantitative values of the derived size distributions, even if the true precision of the DTM remains undefined.

Using the Zevenberg–Thorne approach for slope- and hillshade calculations in Q-GIS, the resulting raster maps enabled the identification of 246 recent and historical landslide scars and for the mapping of the respective detachment areas. Allochthonous landslide deposits were not considered. Since this optical method yields the surface including vegetation, the survey was restricted to nonforested areas.

The 246 detected landslide scars were verified in the field and classified into rotational and translational type according to the scheme of Varnes (1978). Rotational slides were recognized by their short transport distance of a few decimeters and by the property that the sliding masses remained in the failure cavity. Failure escarpments are often characterized by a slightly converging shear plane with a crescent-like shape in plan view and terrace-like curve in cross-sectional view. The sliding masses often tend to become swampy, thus exhibiting noticeably green vegetation cover in comparison with surrounding grasslands. In turn, translational slides were identified by their tendency for higher transport distances and a hollow form with relatively uniform failure depth. In plan view, their detachment areas mostly show irregularly, elongated shapes. Some of the structures form multiarmed shapes. Figure 3 shows an example of a fresh translational slide and an older slide where the scar is already covered by vegetation.

In total, 136 out of 246 slides could be assigned to one of these two types (Table 1). The location and the spatial extent of the landslide scars are shown in Figure 4. Note that the landslides were not classified by age. Only B61 and B105 were evidently created during the heavy rainfall of January 2018. Escarpments of rotational landslides that are not covered by vegetation were found at only a few locations, suggesting the rather recent activity of landslides B2, B27, B42, B73, and B94. Hence, the predominant portion of the landslide inventory is considered to be historical.

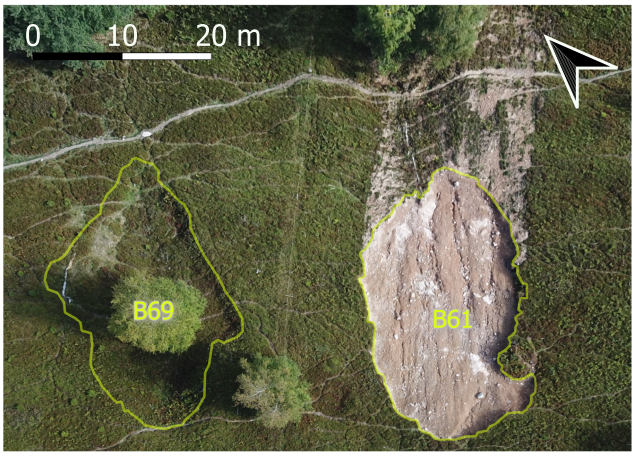

FIGURE 3 Characteristic shapes of translational landslides B69 and B61 at hillslope H1. Landslide B61 occurred during the rainstorm in January 2018. EPSG code for map projection: 32632 [Color figure can be viewed at wileyonlinelibrary.com]

TABLE 1 Number of slope failures on both considered slopes

Landslide type	H1	H3	Total
Rotational	45	46	91
Translational	17	28	45
Unassigned	57	53	110
Total	119	127	246

2.2 | Characterization of the subsurface

For the assessment and calculation of the local stability of slopes, insights into the architecture of the subsurface are essential. Based on the facies of the glacial debris cover (Wimmenauer & Schreiner, 1981), it is expected that the maximum grain size exceeds 63 mm. Investigation of the soil strata by percussion drilling was therefore not feasible. Instead, ground-penetrating radar (GPR) was used to mark the boundary to the bedrock. A detailed review of this method is provided by Neal (2004).

In total, 15 GPR surveys with an overall track length of 1.3 km were carried out in September 2019 and January 2020. A bistatic, common-offset, sled-mounted, unshielded 100-MHz antenna equipped with a pulseEKKO Pro transmitter and a pulseEKKO Ultra receiver unit (Sensors & Software) was used. Preceding in situ measurements with a 200-MHz antenna suffered from rapid signal attenuation and strong dispersive diffraction. Due to the expected lower propagation velocities of 0.04–0.06 m ns^{-1} from this survey and literature data on glacial deposits (Lukas & Sass, 2011), 100-MHz antennas were chosen for this study. The antennas were oriented perpendicular broadside with separation of 0.5 m. Profiles were taken preferentially parallel to the contour lines with a few cross profiles to enable subsequent corroboration of depth migration of individual profiles. Traces along the GPR profiles were recorded at a spacing of 0.2 m, triggered by an odometer wheel attached to the rear of the sled.

The data were recorded with a 240 ns time window, trace stacking of 4096 measurements, and in situ time-zero corrections before the acquisition of each profile. Postprocessing steps were applied using the pulseEKKO software as follows: (i) threshold-based time-zero adjustment, (ii) dewow and band-pass filter, (iii) muting of air and ground waves, and (iv) fitting of the velocity function to the shape and size of visible point source reflections and diffraction. The location of diffraction hyperbolas was carefully noted and the profiles f–k migrated. For interpretation, Spreading & Exponential Compensation (SEC) gain with attenuation of 0.9 db m^{-1} was applied, and the topography was corrected by elevation static correction based on LiDAR and drone photogrammetry data acquired along the profiles.

2.3 | Geotechnical characterization

Geotechnical characterization was not a focus of this study. Thus, only a few analyses were performed, to verify the characteristics of the sediment described by Wimmenauer and Schreiner (1981). Grain size analyses by sieving and settling were conducted according to DIN EN ISO 17892-9 (2016). For this investigation, 12 samples were taken in total at depths from −0.75 to −0.1 m below the subsurface.

The resulting distribution curves (Supplementary Figure S4) were dominated by gravel with a cumulative mass fraction of 48.4 ± 10.9 wt.% and sand with 38.8 ± 7.3 wt.%. Silt contributed a minor fraction of 10.0 ± 3.9 wt.%, whereas clay was almost absent with a content of less than 5 wt.%.

Since the grain size analyses revealed no fundamental differences among the samples, only a single triaxial testing set consisting of three experiments was performed in order to estimate the effective shear parameters after D.I.N.E.N.I.S.O. 17892-9 (2018). To obtain some kind of upper limit for the cohesion, the sample was taken from location B2 with the highest content of clay and silt (about 20% in total) according to the grain size analyses. Fitting of the shear parameters to the Mohr circles of the three experiments (Supplementary Figure S3) yielded an angle of internal friction of $\phi = 38^\circ$ and even a negative cohesion of $C = -1$ kPa. As a test of uncertainty, the parameters were also determined using the combinations of two experiments. Values of $C = -13.0$ kPa, −6.6 kPa, and 8.2 kPa were obtained. So, there is an uncertainty of several kPa even for this single triaxial testing set. As the grain size sample from B2 had the highest content of clay and silt, the cohesion should be even lower at the other locations. As a rough estimate, the cohesion should not be higher than 10 kPa over the entire considered domain.

3 | DATA ANALYSIS AND RESULTS

3.1 | Spatial distribution of landslides

The areas of H1 and H3 exposed to landsliding are located at the foot of the respective hillslope. Even though the planar surfaces of these mapping areas feature slope angles within a quite narrow range between about 20° and 25°, the mapped landslides are not distributed homogeneously. This is revealed by the nesting and staggering of several rotational and translational landslides, such as B1 plus B2 and B49, B61, plus B69 at H1 as well as B90 to B94 and B105 and B108 at H3 (Figure 4). The clustering of these mass movements is most likely triggered by the accumulation of water both above and underneath the surface and is most likely related to formation of gullies (Figure 5).

As an example, B61 at H1 has a concise, crescent-shaped recess at the southern upper edge (Figure 3), suggesting that the fracture formation initially spread from this location since the preexisting cavity of B49 did not provide any resistance to the detachment. A similar mechanism took place at B105 at H3. Over several heavy rainfall events, this process supports the ongoing erosion of gullies at both hillslopes. Due to the intensified water inflow into the sediment layer, a single hollow can cause the activation of newer detachments in the surroundings and even initiate the formation of a new coherent channel system over long times.

3.2 | Landslide size distribution

Figure 6 shows the probability density of the landslide size distribution estimated from the 246 mapped landslides, where the area of ablation is considered as size. The data points were obtained by aligning the data in logarithmic bins where the bin size increases by a factor of $\sqrt{2}$ from one bin to the next.

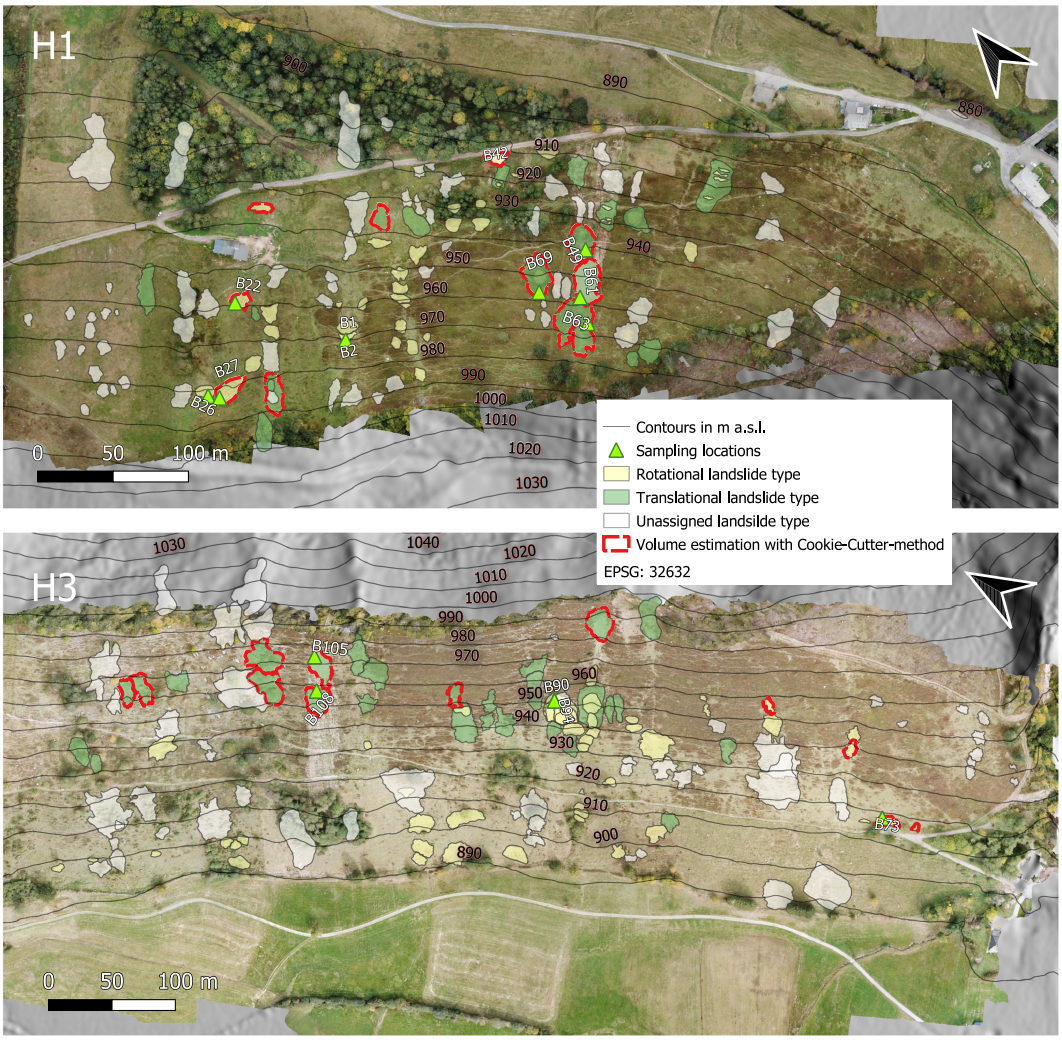

FIGURE 4 Orthophotos derived from quadrocopter overflights with mapped ablation areas of historical and recent landslides [Color figure can be viewed at wileyonlinelibrary.com]

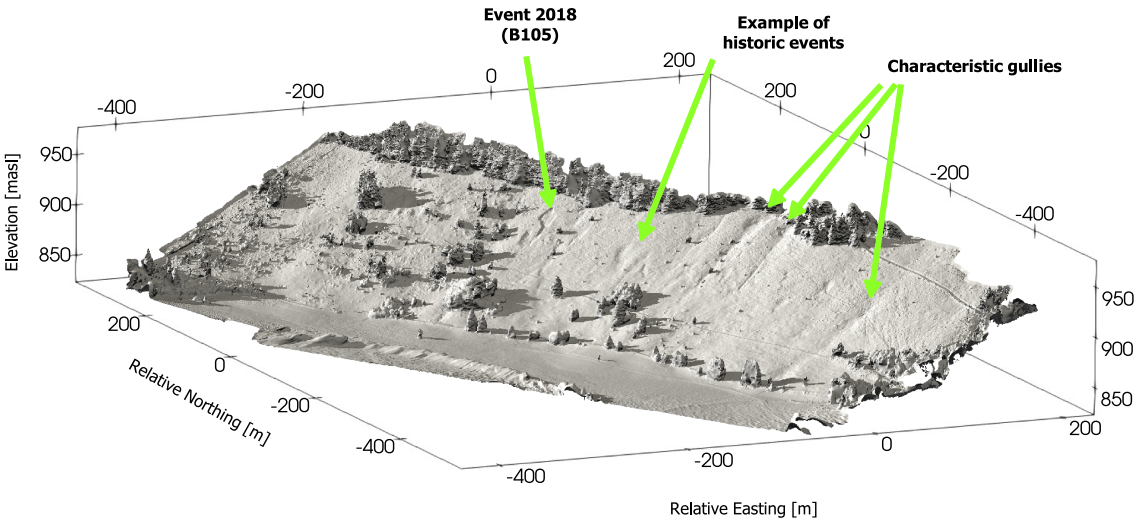

FIGURE 5 Characteristic shapes of gullies at hillslope H3 in the surroundings of historical landslide events [Color figure can be viewed at wileyonlinelibrary.com]

Due to the limited range of areas, a power-law behavior (corresponding to a straight line on a double-logarithmic plot) at large sizes is only recognizable over less than one decade in area. In turn, the rollover at small sizes (Malamud et al., 2004; Stark & Hovius, 2001) is clearly visible. The probability density achieves a local maximum at $A \approx 50$ m^2. The behavior at very small sizes $A < 10$ m^2 is probably owing to the small numbers (four events in the first bin and one event in the second bin), although one of the three large datasets analyzed by Malamud et al. (2004) even showed a systematic increase at very small sizes.

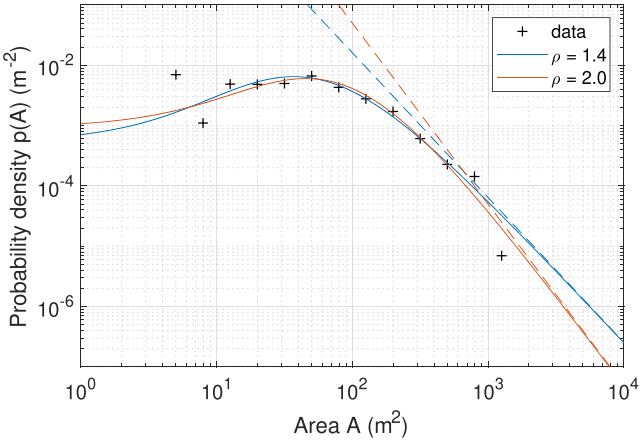

FIGURE 6 Landslide size distribution. The points show the probability density estimated by aligning the mapped landslide sizes in logarithmic bins. The curves correspond to the inverse gamma distribution (Equation (1)) with different parameter values [Color figure can be viewed at wileyonlinelibrary.com]

Early studies (e.g., Hovius et al., 1997) fit a Pareto distribution (a straight line on a double-logarithmic plot) to the part of the inventory above a given minimum landslide size. The rollover at small sizes leads to systematic underestimation of the exponent (the negative slope on a double-logarithmic plot) and thus an overestimation of the frequency of large landslides. Although this problem may not be crucial if the focus is on comparing different datasets (e.g., from different lithologies Hurst et al., 2013), it has become popular to use statistical distributions that take such rollover into account, so that the fit can include the entire dataset. Based on the idea that the rollover arises from incompleteness of the inventory, Stark and Hovius (2001) proposed a double Pareto distribution with an increasing power-law part at small sizes and a decreasing power-law tail. This distribution has also been used in other studies (e.g., Guthrie & Evans, 2004a, 2004b). Malamud et al. (2004) were the first to suggest that the deficit in the frequency of small landslides compared with a Pareto distribution is not a matter of data incompleteness but rather a real property of landslides in soil. They proposed an inverse gamma distribution as a heuristic description of the entire distribution. The probability density of the inverse gamma distribution in terms of area A reads

$$p(A) = \frac{1}{a\Gamma(\rho)}\left(\frac{a}{A-s}\right)^{\rho+1}\exp\left(\frac{a}{A-s}\right), \quad (1)$$

where ρ, a, and s are parameters, and Γ is Euler's gamma function. Similarly to the double Pareto distribution, the inverse Gamma distribution approaches a power law for $A \to \infty$,

$$p(A) \sim A^{-(\rho+1)}. \quad (2)$$

The cumulative distribution, i.e., the probability that a given landslide has an area $\geq A$, also turns into a power law for $A \to \infty$,

$$P(A) = \int_A^\infty p(u)du \sim A^{-\rho}, \quad (3)$$

but with an exponent of ρ instead of $\rho + 1$.

The inverse Gamma distribution has apparently been used more frequently than the double Pareto distribution in recent studies (e.g, Tanyas et al., 2018; Van Den Eeckhaut et al., 2007). A few studies have compared these two distributions (Hurst et al., 2013; Li et al., 2016; Tebbens, n.d.) and found differences in the exponent ρ of up to about 0.4, where the values obtained from the inverse Gamma distribution tend to be higher than those obtained from the double Pareto distribution. However, the small dataset considered in this study prevents a contribution to answering this question of which distribution is more appropriate. As the range of the power-law tail is very small here, both are better than fitting a Pareto distribution to a small part of the dataset only. In the following, we use the inverse Gamma distribution.

Equation (1) can be fit to the data by applying the maximum-likelihood method. This means that the joint probability density of the data is interpreted as the likelihood of the parameter combination (ρ, a, s),

$$L(\rho,a,s) = \prod_i p(A_i), \quad (4)$$

where the product expands over all areas A_i in the dataset. The combination (ρ, a, s) that maximizes L is considered to be the most likely parameter set. Practically, the maximization is performed by minimizing

$$-\ln L(\rho,a,s) = -\sum_i \ln p(A_i). \quad (5)$$

Application to the 246 mapped landslides yields an exponent $\rho = 2.0$ and the other values given in Table 2. The problem is, however, practically underdetermined due to the limited range of landslide sizes. As Malamud et al. (2004) suggested a universal value of $\rho = 1.4$, we also tested the fit when assuming this fixed value, so that only a and s are adjustable parameters. The resulting values are also presented in Table 2, while the resulting probability densities are plotted in Figure 6. Both curves can hardly be distinguished over the range covered by the data. The respective values in $\ln L$ differ by only 0.013, so that the Bayes factor (the ratio of the two L values) is 1.013. This means that the combination with $\rho = 2.0$ is formally more likely by a factor of 1.013 than the version with $\rho = 1.4$, but this difference is so small that the two must be considered equivalent. Therefore, there is no evidence that the exponent deviates from the universal value $\rho = 1.4$ suggested by Malamud et al. (2004).

The distribution as a whole, however, deviates from the predicted distribution at large landslide sizes. The largest landslide in our dataset has an area of $A_{max} = 1096\,m^2$. The probability density estimated from the binned data (points in Figure 6) follows the inverse gamma distribution reasonably well up to about this size and then suddenly drops to zero. In contrast, the cumulative probability $P(A_{max})$ (Equation (3)) is 3.7% for $\rho = 1.4$, so the inverse gamma distribution predicts about nine landslides in the inventory with sizes $A \geq A_{max}$. Thus, the distribution of the data is rather a truncated inverse gamma distribution with a cutoff at a given maximum landslide size. As the maximum-likelihood estimate assumes a full inverse gamma distribution without a cutoff, the lack of large landslides also explains the overestimation of the exponent.

The lack of large landslides on the considered slopes can be quantified with the help of the extreme value distribution where $P_e(A)$ is the probability that the largest landslide in an inventory of n landslides has a size of at least A. This probability can be computed by considering the inverse case that all n landslides are smaller than A, i.e.,

$$1 - P_e(A) = (1 - P(A))^n. \quad (6)$$

Using the relation $\left(1 - \frac{x}{n}\right)^n \to \exp(x)$ for $n \to \infty$, the extreme value distribution can be written in the form

$$P_e(A) = 1 - \exp(-nP(A)) \quad (7)$$

for large n. This distribution is shown in Figure 7, while some of its characteristic values are presented in Table 2.

The probability that the largest event will be larger than the largest observed landslide is $P_e(A_{max}) = 99.99\%$ for $\rho = 1.4$. Even for the estimate $\rho = 2.0$ that is already biased by the cutoff, it is 98.60%, so an inverse gamma distribution without an upper cutoff can be excluded for the size of the largest detected landslide in any case at more than 95% confidence level. For $\rho = 1.4$, the largest landslide should be even larger than $A_{95} = 2510\,m^2$ at 95% probability, which is about 2.3 times as large as the largest detected landslide. The expected size of the largest landslide in an inventory of 246 landslides should be $\overline{A_{max}} = 17{,}660\,m^2$ for an inverse gamma distribution without an upper cutoff at $\rho = 1.4$, which is even 16 times larger than observed.

3.3 | Landslide volume and depth

Detached volumes were estimated for 22 sufficiently preserved cavities. The cookie-cutter tool originally developed for glacial bedforms (Smith et al., 2009) was used for this purpose. This tool first removes the disturbed area from the DEM and then fills the void with a thin plate spline function. As this kind of interpolation is sensitive to elevations and to local slopes close to the boundary of the void, it relies on the preservation of the topography around the cavity. In total, 22 out of the 246 mapped landslides appeared to be visually preserved sufficiently well. A buffer around the cavity was introduced to reduce the effect of alterations in topography. The required width of the buffer was estimated visually for each of the 22 cavities.

TABLE 2 Parameters of the inverse gamma distribution (Equation (1)) and properties of the respective extreme value distribution. The right-hand column refers to the result of the maximum-likelihood estimate for all three parameters. The middle column refers to a maximum-likelihood estimate of a and b only, with a fixed exponent $\rho = 1.4$ as suggested by Malamud et al. (2004)

ρ	1.4	2.0
a (m^2)	129	224
s (m^2)	−16.8	−29.0
$-\ln L(\rho,a,s)$	6.159	6.146
$P(A_{max})$ (%)	3.7	1.7
$P_e(A_{max})$ (%)	99.99	98.60
A_{95} (m^2)	2510	1330
$\overline{A_{max}}$ (m^2)	17660	4298

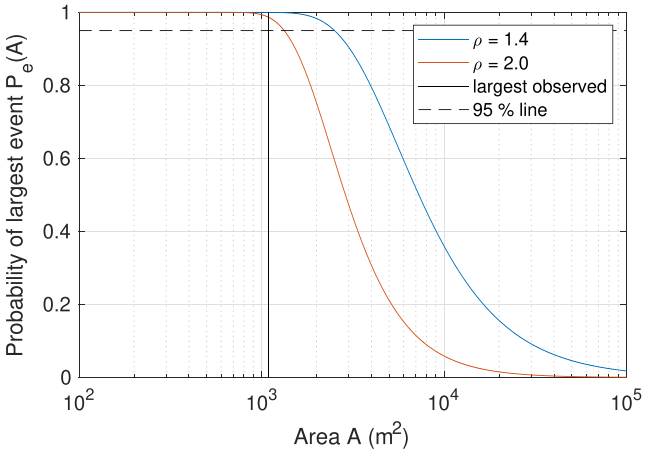

FIGURE 7 Extreme value distribution of landslides sizes for an inventory of $n = 246$ landslides [Color figure can be viewed at wileyonlinelibrary.com]

Figure 8 compares the computed volumes with empirical relations between area and volume, namely the relation

$$V = 0.224A^{1.262} \quad (8)$$

(in meters) obtained by Larsen et al. (2010) from an analysis of 1617 landslide scars and the relation

$$V = 0.074A^{1.45} \quad (9)$$

obtained by Guzzetti et al. (2009) from 677 landslides. Although the exponents in Equations (8) and (9) differ strongly, both relations finally differ by less than 20% in the range between $A = 150\,m^2$ and $A = 1000\,m^2$. Klar et al. (2011) obtained a range from 1.32 to 1.38 for the exponent from theoretical considerations, which lies about in the middle of the two values mentioned above. In the following, we use Equation (8) because it was obtained from a larger dataset.

If the mean landslide depth d is defined as the ratio of volume to area, this relation becomes

$$d = \frac{V}{A} = 0.224A^{0.262}. \quad (10)$$

The volumes estimated for the two fresh (January 2018) landslides (B61 and B105) are in very good agreement with Equation (8), while the majority of the other volumes are up to about three times lower than predicted. As the raw data used by Larsen et al. (2010) show a scatter of about one decade (minimum to maximum volume at constant area), the volumes obtained here may still be reasonable. The volumes of old landslides, however, may also be systematically underestimated. First, the cavity may have been partly filled with sediment over time. Moreover, thin plate splines are sensitive to the slopes at the boundary. If the boundary of an old landslide scar has been smoothed over time, the reconstructed original surface will be too low, so that the volume will also be underestimated. As a systematical underestimation cannot be excluded and the results for the two fresh landslides are very close to the predicted volumes, the evidence

that the landslides considered here are shallower than predicted by Equations (8) and (10) is rather weak, so we assume that these relations capture the scaling properties of the landslides considered here well. For the largest landslide in the inventory ($A_{max} = 1096\,m^2$), the predicted volume is about 1500 m^3, corresponding to a mean depth of about 1.4 m.

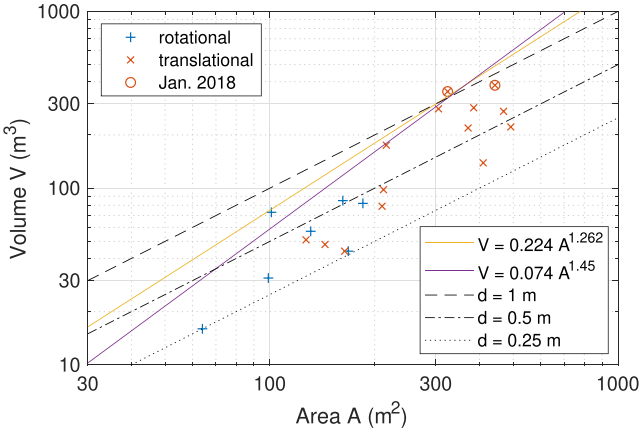

FIGURE 8 Estimated landslide volumes. Data points were obtained using the cookie-cutter tool (Smith et al., 2009). The orange line shows the relation suggested by Larsen et al. (2010). The dashed lines correspond to given mean depths [Color figure can be viewed at wileyonlinelibrary.com]

3.4 | Assessment of the subsurface structure

The interpretation of the GPR profiles was approached by distinguishing different radar facies (Jol & Bristow, 2003). Based on reflection patterns, three different facies were determined (Figures 9 and 10). The lowermost radar facies RF3 is interpreted as the bedrock, characterized by a few subparallel linear reflectors, an absence of point reflectors, and strong signal attenuation with respect to similar two-way travel times in all the profiles. The upper section shows multiple point reflections and segments with strong echoing events (Figure 9, profile 13 at 52–60 m). The partly very coarse-grained glacial sediments contain a multitude of point reflectors that scatter the emitted signal irregularly and cause echoes at neighboring objects, which locally leads to a noisy signal. Also, some echoing is developed at topographic troughs, which we interpret as filled gullies.

Since some of the profiles (e.g., Figure 10) show an additional subhorizontal reflector, indicating stratification within the glacial sediments (Figure 10, profile 3 from 20 m on), the upper section is further subdivided into two radar facies RF1 and RF2, with RF2 always being separated from the lower section RF3 by a distinct, continuous reflector. We assume that the textural change from the glacial deposits to the underlying bedrock causes this strong contrast in relative dielectric permittivity that is responsible for the reflection (Sucre et al., 2011; van Dam & Schlager, 2000). The onset of the lower reflector at

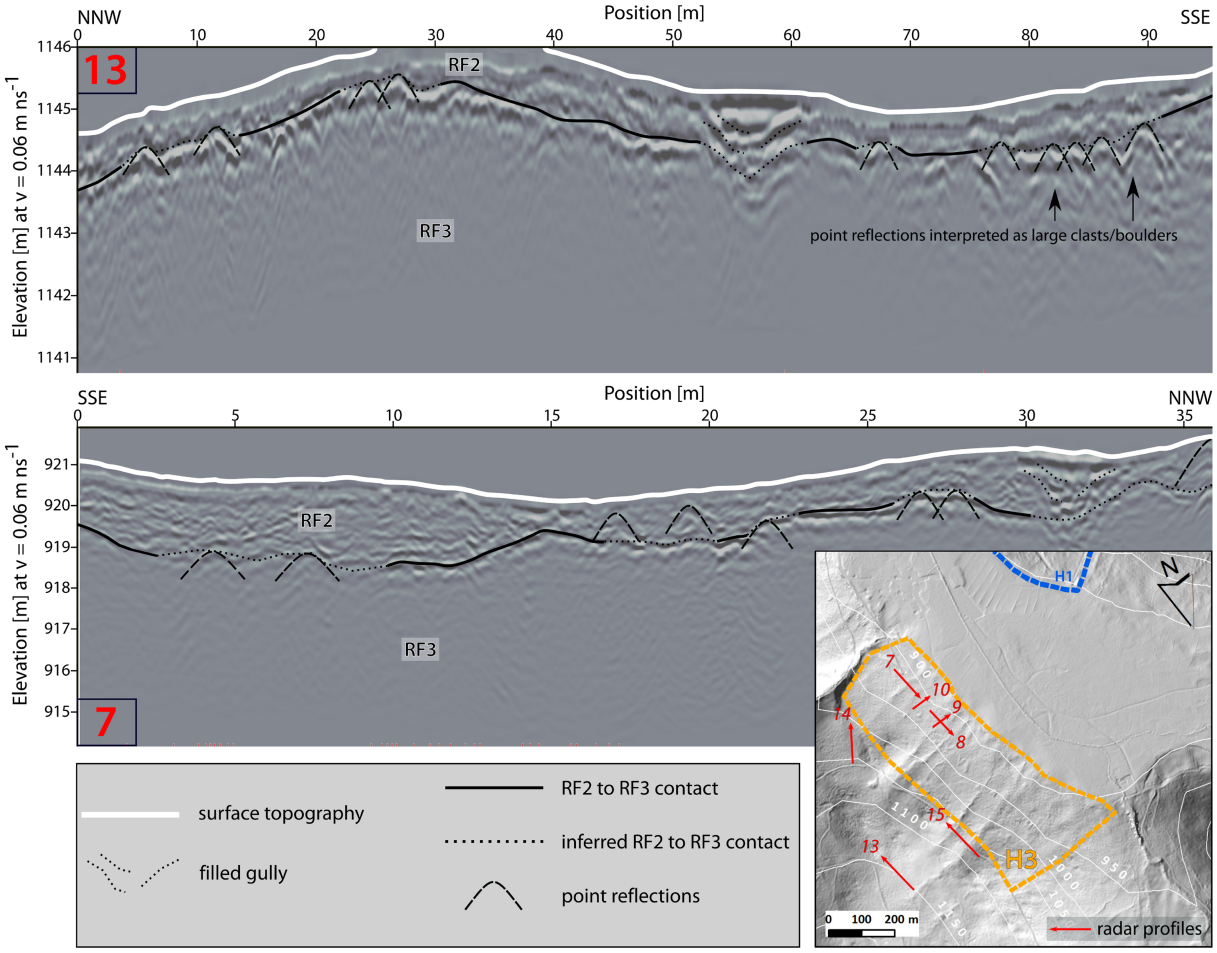

FIGURE 9 GPR profiles 7 and 13 at site H3 with their respective orientation. RF2 and RF3 are the radar facies interpreted in profile 3 and 6. Note the apparent formation and refilling of gullies, as well as abundant point reflectors in the upper section [Color figure can be viewed at wileyonlinelibrary.com]

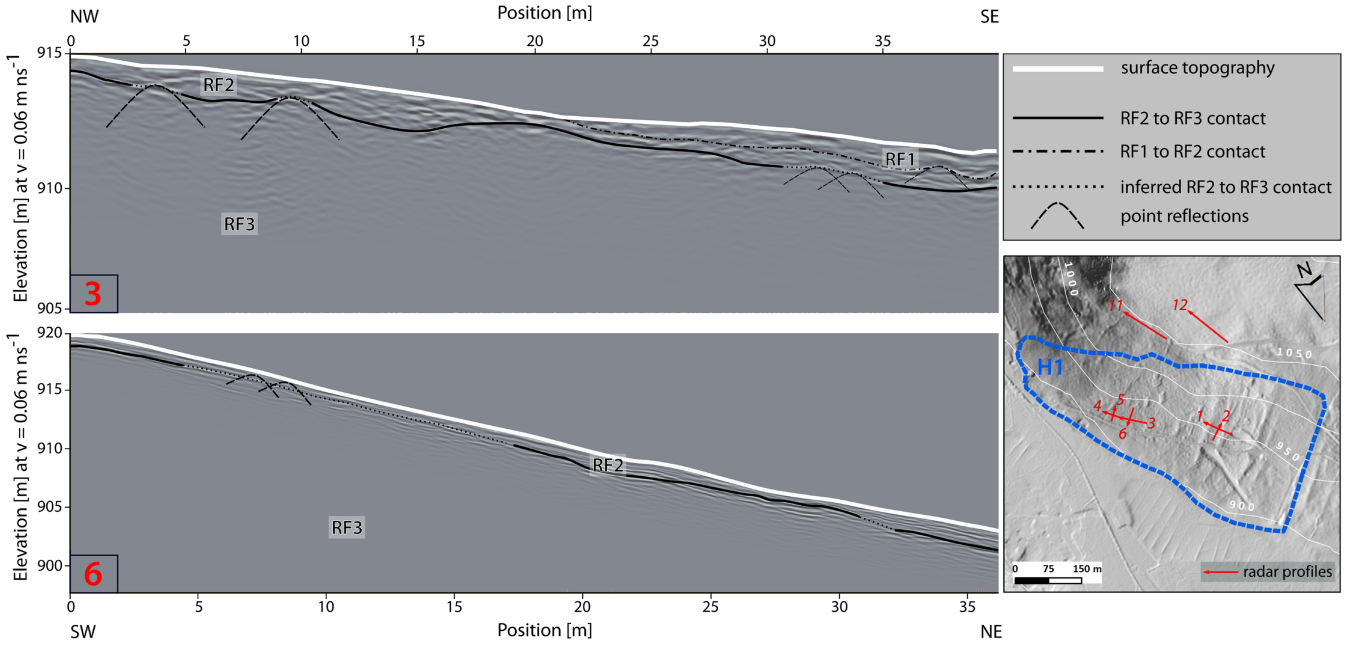

FIGURE 10 GPR profiles 3 and 6 at the southwestern hillslope H1. Radar facies 1 and 2 (RF1 and RF2) represent glacial sediments. Radar facies 3 (RF3), marked by strong signal attenuation and a lack of diffraction hyperbolas, is interpreted as the bedrock. Depth to bedrock values were determined from the solid marked boundary of RF2 to RF3 [Color figure can be viewed at wileyonlinelibrary.com]

the top of RF3 is interpreted below as depth to bedrock, i.e., the transition from glacial deposits (soil) to bedrock.

Adjustment to the reflection parabolas yields two-way travel time velocities between $v = 0.06\,\mathrm{m\,ns^{-1}}$ and $v = 0.08\,\mathrm{m\,ns^{-1}}$ in all profiles. Velocities of $v = 0.06\,\mathrm{m\,ns^{-1}}$ were consistently determined in RF1 and RF2, but predominantly higher apparent velocities were present in RF3. In comparison, Tillard and Dubois (1995) determined two-way velocities of about $0.12\,\mathrm{m\,ns^{-1}}$ at an emission frequency of 200 MHz in granitic rock, indicating higher characteristic EM wave velocities for granitic rocks and effectively low penetration ability in the present study. Based on these results, we assumed a velocity of $v = 0.06\,\mathrm{m\,ns^{-1}}$ to transform two-way travel times into depths.

For the identified contacts, the depth to bedrock was determined in intervals of 2 m horizontally and 0.1 m vertically. Because the bedrock is not fully traceable through all profiles, we differentiate between "inferred contact" and "contact," as indicated in Figures 9 and 10, and discard inferred contacts from later analysis.

A simple approach was chosen for analyzing the depths to bedrock obtained from the GPR survey along the profiles. The profiles were rasterized using 5 × 5 m pixels, and a mean depth was computed for each pixel that contained data. These were 95 pixels in total. The resolution of 5 m is a tradeoff between obtaining a sufficient number of pixels and reducing the influence of small-scale variations in depth that are not relevant to slope stability. The obtained statistical distribution is shown in Figure 11. The largest depth found on this scale is 2.2 m.

The data tentatively suggest that the depths at H1 are slightly higher than at H3, but lower at the profiles outside the regions H1 and H3 (cf. Figure 1). As the outside profiles are in the upper parts of the slopes, the latter results could reflect an increase of thickness in downslope direction due to long-term downward movement of material. However, note that the profiles cover only a small part of the total area and are not necessarily representative. Regression-based models for estimating soil thickness (e.g., Olyphant et al., 2016; Segoni et al., 2012) might help here. However, the slopes considered here are topographically quite homogeneous, so the application of such a model would require an independent validation that would go beyond the scope of this study. Therefore, the results of the GPR study tentatively suggest that about 50% of the area has a depth to bedrock of 1 m or less, about 30% a depth of 1.4 m or more, and less than 10% a depth of at least 2 m.

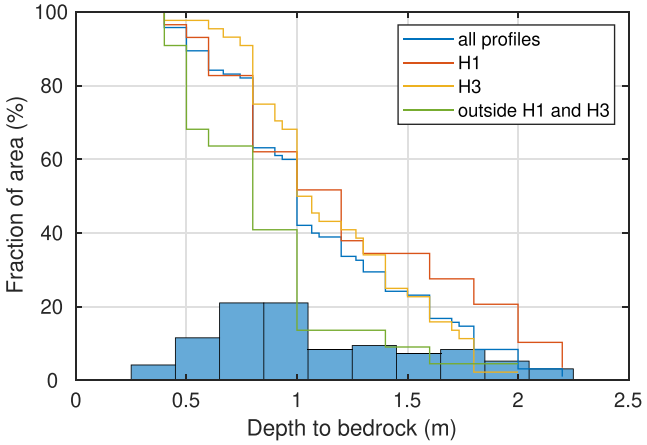

FIGURE 11 Statistical distribution of depths to bedrock obtained from rasterizing GPR profiles. Area is given as a fraction, i.e., the number of pixels per total number of pixels. Bars indicate 0.2 m bins for the entire dataset. Lines describe the cumulative distribution, i.e., the fraction of area with depth greater or equal to the value on the *x*-axis [Color figure can be viewed at wileyonlinelibrary.com]

4 | DISCUSSION

The landslide size statistics of the two slopes considered in this study are overall consistent with the distribution obtained by Malamud et al. (2004) from inventories covering larger scales. Some differences,

however, occur at both small and large landslide sizes. We obtained parameter values $a = 129\,m^2$ and $s = -16.8\,m^2$ describing the rollover of the distribution at small sizes. The respective values $a = 1280\,m^2$ and $s = -132\,m^2$ obtained by Malamud et al. (2004) are about one order of magnitude higher. Hurst et al. (2013) obtained $a = 10{,}900\,m^2$ and $b = -1910\,m^2$ from an inventory of 8453 landslides in the UK, although for the deposit areas and with a lower value of the exponent ρ. The ratio of a and s that describes the shape of the curve is similar in the three inventories. Therefore, the difference mainly lies in the absolute scale at which landslides become less likely with decreasing size. The landslide size with the highest frequency density is about $50\,m^2$ in our inventory, about 400Âž,m^2 in the inventory of Malamud et al. (2004), and about $3000\,m^2$ in the inventory analyzed by Hurst et al. (2013). Among the inventories reviewed by Van Den Eeckhaut et al. (2007), those analyzed by Malamud et al. (2004) had the lowest rollover landslide size. In turn, the data of Van Den Eeckhaut et al. (2007) obtained from an inventory in the Flemish Ardennes did not show a rollover at sizes above $100\,m^2$, but a decreasing power-law section with a smaller exponent for $A \leq 10{,}000\,m^2$. Thus, the rollover in these data must be at $A < 100\,m^2$, although it cannot be seen in the data restricted to sizes above $100\,m^2$.

So, the rollover found in our inventory occurs at sizes about one order of magnitude lower than found by Malamud et al. (2004) and even more than one order of magnitude lower than those found in other studies. This difference may be related to the mechanical properties of the material involved, as the slopes considered here are covered by material with low cohesion. As discussed above, cohesion avoids shallow failure and thus inhibits small landslides. The potential influence of this effect on the rollover in the landslide size distribution was discussed in detail by Li et al. (2014) and was even suggested to be the primary reason for the rollover at small sizes. So, the low cohesion found here provides an explanation for the shift of the rollover towards small sizes compared with other inventories, at least qualitatively.

A rough quantitative estimate can be obtained by assuming a slope-parallel failure plane at a depth d (normal to the surface) below a straight slope with a slope angle α. The normal stress is then $\sigma = wd\cos\alpha$, where w is the specific weight of the soil. The critical shear stress is thus

$$\tau_c = \sigma \tan\phi + C = wd\cos\alpha \tan\phi + C, \quad (11)$$

where ϕ and C are the angle of internal friction and the cohesion, respectively. So, cohesion results in a relative increase in the critical shear stress and thereby in the safety factor by a multiple of

$$\epsilon = 1 + \frac{C}{wd\cos\alpha\tan\phi}. \quad (12)$$

The rollover occurs at landslide sizes of about 50 m^2, and the frequency density is reduced by about one order of magnitude compared with the extrapolated power law (Figure 6). Equation (10) predicts a mean landslide depth of 0.62 m at this size. Assuming $w = 15\,kN\,m^{-3}, \phi = 38^\circ$ (Supplementary Figure S3), and $\alpha = 22^\circ$, Equation (12) predicts an increase in the safety factor by a multiple of 1.15 at $C = 1\,kPa$ and by a factor of 1.74 at $C = 5\,kPa$. In turn, no strong deviation from the power law is observed at $A = 500\,m^2$. Equation (12) predicts an increase by a factor of 1.08 and 1.4 at these two values of C. So, potential landslides with $A = 50$Âž,m^2 are more stable by only a factor of 1.06 compared with those with $A = 500\,m^2$ at $C = 1\,kPa$, but by a factor of 1.25 at $C = 5\,kPa$. Considering that the range of 1–1.3 is often considered to be the conditionally unstable regime, a change by a factor of 1.25 could indeed cause a strong difference in landslide frequency. Thus, a cohesion on the order of magnitude of 5 kPa could be responsible for the rollover in the distribution with a maximum probability density at sizes of about $50\,m^2$ found in this study. However, it was not conceivable at the time when the field and laboratory work was performed that a more precise estimate of the cohesion would become relevant. Anyway, it would have been a challenge to determine whether the cohesion was greater than 5 kPa for a considerable part of the domain, even with a larger number of samples.

While our results support the hypothesis that the cohesion is responsible for the rollover, the alternative hypothesis of undersampling cannot be discarded. As discussed above, the landslide volumes estimated from the topography were consistent with the prediction from Equation (8) only for the two recent landslides. The volumes of older landslides were presumably underestimated due to changes in small-scale topography, which could also affect the detectability in the field and in DEMs. Compared with other studies where a rollover at larger sizes was found, our study refers to smaller scales with a better detectability of small landslides and to soils with a low cohesion. As both differences probably have similar effects on the location of the rollover, an influence of undersampling still cannot be refuted. Nevertheless, our results support the theoretical consideration of Li et al. (2016) about the influence of cohesion and the original conjecture of Malamud et al. (2004) that the rollover is real.

At this point, one may ask whether the cohesion in combination with variations in soil thickness may also be responsible for the concentration of the landslides in the lower parts of the slopes, although the entire slopes are rather homogeneous in terms of slope angle. The results of Sect. 1 suggest that flow and accumulation of water in the subsurface may be responsible for the higher susceptibility of the lower parts. This hypothesis is supported by the analysis of the topography, in particular by the occurrence of gullies. However, the analysis of the subsurface structure (Sect. 1) indeed revealed a greater depth to bedrock at the two areas H1 and H3 compared with the areas above these domains (Figure 11). The mean depths of the profiles at both H1 and H3 are about 1.2 m, while the mean depth of those outside H1 and H3 is only 0.9 m. However, the difference in the factor of safety between these two depth would be only about 3% for $C = 1\,kPa$ and about 9% for $C = 5\,kPa$ according to Equation (12). So, the concentration of landslides in the lower slope segments is probably not an immediate effect of an increase in soil depth in downslope direction. Although vegetation may also have an influence on the distribution, the accumulation of water in the subsurface remains the most likely reason for the strong increase of landslide susceptibility in downslope direction.

The most important difference in the landslide statistics, however, concerns the tail of the distribution, i.e., the number of large landslides. We found a maximum size of about 1100 m^2, while the assumed inverse gamma distribution predicts a maximum size of at least 2500 m^2 even at 95% probability (Figure 7). So, there is a clear lack of large landslides despite the good agreement with the predicted

distribution at smaller landslides. As discussed above, the mean depth of landslides of the maximum size found here should be about 1.4 m. The results of the GPR measurements (Figure 11) suggest that the rather low depths to the bedrock may be the reason for the limited landslide sizes. Even on the considered 25 m^2 pixel scale, less than one-third of the area has a depth of at least 1.4 m, and depths of 2 m or more are very rare. The largest expected landslide with an area of $\bar{A}_{max} = 17{,}660\,m^2$ should have a mean depth of about 2.9 m according to Equation (10), which is even 30% larger than the maximum depth to bedrock of 2.2 m found among the considered 25 m^2 pixels. So, it is likely that the lack of landslides much larger than 1000 m^2 is due to an insufficient depth of potentially mobile material.

A cutoff in the distribution at large landslide sizes was presumably discussed first by Hergarten (2012) in the context of landslides in rock. Topography was suggested as the limiting factor there. Hurst et al. (2013) observed a deficit in the number of large landslides in soils at areas on the order of magnitude of 1 km^2 and also attributed this to topography. In our study, however, the maximum landslide size is several orders of magnitude smaller than the size of the slopes. So, the limited soil thickness introduces a cutoff at much lower scales than considered by Hurst et al. (2013).

From a practical point of view, the implications of this result for hazard assessment are very interesting. Although we were not able to assign an age to the majority of the mapped landslides, it is obvious from the pattern of the landslides alone (Figure 4) that the landslide susceptibility at the considered location is rather high. The slopes are quite steep, but covered by a potentially mobile layer that is only weakly supported by cohesion. The observed landslides are, however, rather small. While landslides of the observed sizes will typically not have much effect, the question is whether larger landslides causing serious damage to infrastructure or even loss of life could occur here. This question becomes particularly relevant it either the frequency or intensity of heavy rainstorms increases, or if a larger part of the winter precipitation changes from snow to rainfall.

In general, the resulting increase in landslide frequency is accompanied by an increasing size of the largest landslide to be expected in a given time span. As an example, the extreme value distribution of the inverse gamma distribution predicts an expected maximum size of $\bar{A}_{max} = 17{,}660\,m^2$ (Table 2) for a sample size of $n = 246$ landslides as found in our study. If we increase the sample size to $2n = 492$ landslides, the expected maximum landslide size increases to $\bar{A}_{max} = 29{,}000\,m^2$. This is, however, only true for the original distribution without any cutoff. Given that the observed cutoff at $A \approx 1100\,m^2$ is indeed imposed by the geological constraint of limited soil thickness, it cannot be expected that this cutoff will be strongly affected by climate change. In this case, an increasing frequency or intensity of rainstorms may have an effect on landslide frequency, but the maximum landslide size to be expected should not increase much. This result should also hold for locations with a similar setting, i.e., with steep slopes covered by a thin soil cover.

Determining a maximum possible landslide size or at least the size above which landslides become rapidly less likely would be a major step in hazard assessment. As mentioned above, the largest landslide observed at the considered location has an expected mean depth of 1.4 m, and about 30% of the area has a soil thickness of at least 1.4 m. It might be tempting to derive a relationship between the maximum landslide size and any quantile of the soil thickness or even the mean soil thickness. However, these data are based on a single landslide on slopes where the soil depth has been investigated for only a small fraction of the area. An analysis of the respective largest landslide in several inventories with known soil depths would be necessary to obtain a robust relationship. Such a relationship could finally improve hazard assessment in combination with future developments such as drone-based GPR systems, satellite-based sensors, or improved mathematical models for predicting soil thickness.

CONCLUSIONS

This study focused on the spatial pattern and size distribution of soil-borne landslides in the submountainous area of the Black Forest, Germany. Geophysical surveying (GPR) revealed that the two steep slopes investigated bear only a thin soil layer of about 1 m, consisting of unconsolidated glacial sediments with low cohesion. While the analyses of size statistics derived from DEM and orthophotos are overall consistent with the distribution recognized in larger inventories, our study reveals differences from previous studies at both small and large landslide sizes.

First, we observed a rather high proportion of small landslides. The rollover in the distribution occurs at an area of about 50 m^2, which is about one order of magnitude lower than the rollover found in other inventories. This difference is likely explained by the low cohesion, since cohesion inhibits small landslides in general. For the considered inventory, a low cohesion of about 5 kPa would be able to explain the rollover. This result supports the hypothesis that cohesion plays a major part in the deficit of small landslides (Li et al., 2014; Malamud et al., 2004) observed in several studies, although an effect of undersampling still cannot be excluded.

As a second result, we observed a distinct cutoff in the distribution at large landslide sizes. In this study, it was found at a size of about 1100 m^2, which is considerably lower than the cutoff found by Hurst et al. (2013) in larger inventories. This cutoff is probably due to the limited soil thickness. In contrast to the increased frequency of small landslides, the cutoff at large landslide sizes has a direct impact on hazard assessment. In particular, this result suggests that an increase in the frequency and intensity of rainstorms or a shift of winter precipitation towards rainfall should predominantly result in an increase of landslide frequency, but without increasing the size of the largest landslides to be expected at the considered location. This result may by transferable to locations with steep slopes and low soil thickness. In this context, the contribution of large landslides to total landslide hazard may be overestimated if soil thickness is not taken into account, in particular if the present-day hazard is projected to future scenarios. However, more research on landslide inventories and on estimating soil thickness is required on the way towards estimating the maximum landslide size to be expected in a given geological setting.

ACKNOWLEDGEMENT

The data that support the findings of this study are available from the corresponding author upon reasonable request.

None of the authors declares any real or perceived financial conflicts of interest.

The authors thank Michael Vandrey, Bertram Schrade, and Wolfgang Gleim from HPC AG Freiburg (Germany) for the idea for this project, their kind support, and their valuable know-how in

geotechnical skills. We also thank Johann Meier, Hans-Jörg Meier, Adrian Probst, and Benno Kaiser from the Locality of St. Blasien as well as Menzenschwand for their interest in and support of this study. The realization of the triaxial experiments was supported by expert knowledge and professional consultation of Matthias Pamler from Geomation GmbH (Germany).

DATA AVAILABILITY STATEMENT

The data supporting the findings of this study are available from the corresponding author upon reasonable request.

ORCID

Jakob Wilk https://orcid.org/0000-0002-2605-9444
Stefan Hergarten https://orcid.org/0000-0002-4780-284X

REFERENCES

Agisoft LLC. (2018) Agisoft Metashape User Manual: Professional Edition, Version 1.5. Available from: https://www.agisoft.com/pdf/metashape-pro_1_5_en.pdf

Alvioli, M., Guzzetti, F. & Rossi, M. (2014) Scaling properties of rainfall induced landslides predicted by a physically based model. *Geomorphology*, 213, 38–47.

Bak, P. (1996) *How nature works – the science of self-organized criticality*. Berlin, Heidelberg, NY: Copernicus, Springer.

Bak, P., Tang, C. & Wiesenfeld, K. (1987) Self-organized criticality. An explanation of 1/f noise. *Physical Review Letters*, 59, 381–384.

Bell, R., Kruse, J.-E., Garcia, A., Glade, T. & Hördt, A. (2006) Subsurface investigations of landslides using geophysical methods: geoelectrical applications in the Swabian Alb (Germany). *Geographica Helvetica*, 61(3), 201–208.

Brunetti, M.T., Guzzetti, F. & Rossi, M. (2009) Probability distribution of landslide volumes. *Nonlinear Processes in Geophysics*, 16, 179–188.

Chacón, J., Irigaray, C., Fernández, T. & El Hamdouni, R. (2006) Engineering geology maps: landslides and geographical information systems. *Bulletin of Engineering Geology and the Environment*, 65, 341–411.

Crosta, G. (1997) Regionalization of rainfall thresholds: an aid to landslide hazard evaluation. *Environmental Geology*, 35, 131–145.

Crozier, M.J. (2010) Deciphering the effect of climate change on landslide activity: A review. *Geomorphology*, 124, 260–267.

D.I.N.E.N.I.S.O. 17892-9. (2018) Geotechnische Erkundung und Untersuchung – Laborversuche an Bodenproben – Teil 9: Konsolidierte triaxiale Kompressionsversuche an wassergesättigten Böden.

DIN EN ISO 17892-9. (2016) Geotechnische Erkundung und Untersuchung – Laborversuche an Bodenproben – Teil 4: Bestimmung der Korngröenverteilung. Beuth Verlag, Berlin.

DWD (2019) Historische stündliche Stationsmessungen der Niederschlagshöhe für Deutschland Version v006. Deutscher Wetter Dienst – Climate Data Center (CDC). Retrieved from: ftp://ftp-cdc.dwd.de.

Damm, B., Becht, M., Varga, K. & Heckmann, T. (2010) Relevance of tectonic and structural parameters in Triassic bedrock formations to landslide susceptibility in quaternary hillslope sediments. *Quaternary International*, 222, 143–152.

Damm, B. & Klose, M. (2015) The landslide database for Germany: Closing the gap at national level. *Geomorphology*, 249, 82–93.

Damm, B., Varga, K., Heckmann, T. & Becht, M. (2009) The impact of bedrock stratification on landslide susceptibility – an example of GIS-based landslide modelling in the Bunter Sandstone areas of northern Hesse and southern Lower Saxony (Germany). *Die Erde*, 140(1), 175–193.

Densmore, A.L., Ellis, M.A. & Anderson, R.S. (1998) Landsliding and the evolution of normal-fault-bounded mountains. *Journal of Geophysical Research*, 103, 15203–15219.

Drossel, B. & Schwabl, F. (1992) Self-organized critical forest-fire model. *Physical Review Letters*, 69, 1629–1632.

Frattini, P. & Crosta, G.B. (2013) The role of material properties and landscape morphology on landslide size distributions. *Earth and Planetary Science Letters*, 361, 310–319.

Fuyii, Y. (1969) Frequency distribution of the magnitude of landslides caused by heavy rainfall. *Seismological Society of Japan*, 22, 244–247.

Gariano, S.L. & Guzzetti, F. (2016) Landslides in a changing climate. *Earth-Science Reviews*, 162, 227–252.

Geyer, O.F. & Gwinner, M.P. (2011) *Geologie von Baden-Württemberg*. Schweizerbart'sche Verlagsbuchhandlung: Stuttgart.

Gutenberg, B. & Richter, C.F. (1954) *Seismicity of the earth and associated phenomenon*, 2. Princeton University Press: Princeton.

Guthrie, R.H. & Evans, S.G. (2004a) Analysis of landslide frequencies and characteristics in a natural system, coastal British Columbia. *Earth Surface Processes and Landforms*, 29, 1321–1339.

Guthrie, R.H. & Evans, S.G. (2004b) Magnitude and frequency of landslides triggered by a storm event, Loughborough Inlet, British Columbia. *Natural Hazards and Earth System Sciences*, 4, 475–483.

Guzzetti, F., Ardizzone, F., Cardinali, M., Rossi, M. & Valigi, D. (2009) Landslide volumes and landslide mobilization rates in Umbria, central Italy. *Earth and Planetary Science Letters*, 279, 222–229.

Hantke, R. & Rahm, G. (1976) Das frühe Spätglazial in den Quellästen der Alb (Südlicher Schwarzwald). *Vierteljahrsschrift der Naturforschenden Gesellschaft in Zürich*, 121, 293–299.

Hergarten, S. (2002) *Self-organized criticality in Earth systems*. Springer: Berlin, Heidelberg, New York.

Hergarten, S. (2004) Aspects of risk assessment in power-law distributed natural hazards. *Natural Hazards and Earth System Sciences*, 4, 309–313.

Hergarten, S. (2012) Topography-based modeling of large rockfalls and application to hazard assessment. *Geophysical Research Letters*, 39, L13402.

Hergarten, S. & Neugebauer, H.J. (1998) Self-organized criticality in a landslide model. *Geophysical Research Letters*, 25, 801–804.

Hovius, N., Stark, C.P. & Allen, P.A. (1997) Sediment flux from a mountain belt derived by landslide mapping. *Geology*, 25, 231–234.

Hurst, M.D., Mudd, S.M., Attal, M. & Hilley, G. (2013) Hillslopes record the growth and decay of landscapes. *Science*, 341, 868–871.

Jeandet, L., Steer, P., Lague, D. & Davy, P. (2019) Coulomb mechanics and relief constraints explain landslide size distribution. *Geophysical Research Letters*, 46, 4258–4266.

Jensen, H.J. (1998) *Self-organized criticality – emergent complex behaviour in physical and biological systems*. Cambridge University Press: Cambridge, New York, Melbourne.

Jol, H.M. & Bristow, C.S. (2003) Gpr in sediments: advice on data collection, basic processing and interpretation, a good practice guide. *Geological Society, London, Special Publications*, 211(1), 9–27.

Keefer, D.K. (1994) The importance of earthquake-induced landslides to long-term slope erosion and slope failure hazards in seismically active regions. *Geomorphology*, 10, 265–284.

Klar, A.E., Aharonov, E., Kalderon-Asael, B. & Katz, O. (2011) Analytical and observational relations between landslide volume and surface area. *Journal of Geophysical Research*, 116, F02001.

Klose, M., Highland, L., Damm, B. & Terhorst, B. (2014) Estimation of direct landslide costs in industrialized countries: Challenges, concepts, and case study. In *Landslide science for a safer geoenvironment*, Sassa, K., Canuti, P. & Yin, Y. (eds), Springer: Cham; pp. 661–667.

Klose, M., Maurischat, P. & Damm, B. (2015) Landslide impacts in Germany: A historical and socioeconomic perspective. *Landslides*, 13, 183–199.

Krenn, R. & Hergarten, S. (2009) Cellular automaton modelling of lightning-induced and man made forest fires. *Natural Hazards and Earth System Sciences*, 9, 1743–48.

Larsen, I.J., Montgomery, D.R. & Korup, O. (2010) Landslide erosion controlled by hillslope material. *Nature Geoscience*, 3(4), 247–251.

Li, L., Lan, H. & Wu, Y. (2014) The volume-to-surface-area ratio constrains the rollover of the power law distribution for landslide size. *European Physical Journal Plus*, 129(5), 89.

Li, L., Lan, H. & Wu, Y. (2016) How sample size can effect landslide size distribution. *Geoenvironmental Disasters*, 3(1), 18.

Liucci, L., Melelli, L., Suteanu, C. & Ponziani, F. (2017) The role of topography in the scaling distribution of landslide areas: A cellular automata modeling approach. *Geomorphology*, 290, 236–249.

Lukas, S. & Sass, O. (2011) The formation of Alpine lateral moraines inferred from sedimentology and radar reflection patterns: a case study from Gornergletscher, Switzerland. *Geological Society, London, Special Publications*, 354(1), 77–92.

Malamud, B.D., Morein, G. & Turcotte, D.L. (1998) Forest fires: an example of self-organized critical behavior. *Science*, 281, 1840–1842.

Malamud, B.D., Turcotte, D.L., Guzzetti, F. & Reichenbach, P. (2004) Landslide inventories and their statistical properties. *Earth Surface Processes and Landforms*, 29, 687–711.

Meunier, P., Hovius, N. & Haines, A.J. (2007) Regional patterns of earthquake-triggered to ground motion landslides and their relationto ground motion. *Geophysical Research Letters*, 34, L20408.

Neal, A. (2004) Ground-penetrating radar and its use in sedimentology: principles, problems and progress. *Earth-Science Reviews*, 66(3–4), 261–330.

Neuhäuser, B. & Terhorst, B. (2007) Landslide susceptibility assessment using "weights-of-evidence" applied to a study area at the Jurassic escarpment (SW-Germany). *Geomorphology*, 68(1), 12–24.

Nie, W., Krautblatter, M., Leith, K., Thuro, K. & Festl, J. (2017) A modified tank model including snowmelt and infiltration time lags for deep-seated landslides in alpine environments (Aggenalm, Germany). *Natural Hazards and Earth System Sciences*, 17, 1595–1610.

Olyphant, J., Pelletier, J.D. & Johnson, R. (2016) Topographic correlations with soil and regolith thickness from shallow-seismic refraction constraints across upland hillslopes in the Valles Caldera, New Mexico. *Earth Surface Processes and Landforms*, 41, 1684–1696.

Pflug, R. (1982) *Bau und Entwicklung des Oberrheingrabens*. Wissenschaftliche Buchgesellschaft: Darmstadt.

Rahm, G. (1970) Die Vergletscherungen des Schwarzwaldes im Vergleich zu denjenigen der Vogesen. *Alemannisches Jahrbuch*, 1966/67, 257–272.

Segoni, S., Rossi, G. & Catani, F. (2012) Improving basin scale shallow landslide modelling using reliable soil thickness maps. *Nat. Hazards*, 61, 85–101.

Smith, M.J., Rose, J. & Gousie, M.B. (2009) The Cookie Cutter: a method for obtaining a quantitative 3D description of glacial bedforms. *Geomorphology*, 108(3–4), 209–218.

Stark, C.P. & Hovius, N. (2001) The characterization of landslide size distributions. *Geophysical Research Letters*, 28, 1091–1094.

Sucre, E., Tuttle, J.W. & Fox, T.R. (2011) The use of ground-penetrating radar to accurately estimate soil depth in rocky forest soils. *Forest Science*, 57, 59–66.

Tanyas, H., Allstadt, K.E. & van Westen, C.J. (2018) An updated method for estimating landslide-event magnitude. *Earth Surface Processes and Landforms*, 43, 1836–1847.

Tebbens, S.F. (2020) Landslide scaling: A review. *Earth And Space Science*, 7(1), e2019EA000662. https://doi.org/10.1029/2019EA000662

Tillard, S. & Dubois, J.-C. (1995) Analysis of GPR data: Wave propagation velocity determination. *Journal of Applied Geophysics*, 33(1–3), 77–91.

van Dam, R.L. & Schlager, W. (2000) Identifying causes of ground-penetrating radar reflections using time-domain reflectometry and sedimentological analyses. *Sedimentology*, 47(2), 435–449.

Van Den Eeckhaut, M., Poesen, J., Govers, G., Verstraeten, G. & Demoulin, A. (2007) Characteristics of the size distribution of recent and historical landslides in a populated hilly region. *Earth and Planetary Science Letters*, 256, 588–603.

Varnes, D.J. (1978) Slope movement types and processes. In: Schuster, R. L. & Krizek, R.J. (Eds.) *Landslides, analysis and control*. Washington, D.C.: Transportation research board, National Academy of Sciences, pp. 11–33.

Wimmenauer, W. & Schreiner, A. (1981) *Geologische Karte von Baden-Württemberg 1:25 000, Erläuterungen zu Blatt 8114 Feldberg (Schwarzwald). Analoge Ausgabe*. Stuttgart: Geologisches Landesamt Baden-Württemberg & Landesvermessungsamt Baden-Württemberg.

Zienert, A. & Fezer, F. (1967) Vogesen-und Schwarzwald-Kare. *Eiszeitalter & Gegenwart – Quaternary Science Journal*, 18(1), 51–75.

SUPPORTING INFORMATION

Additional supporting information may be found in the online version of the article at the publisher's website.

How to cite this article: Büschelberger, M., Wilk, J., Hergarten, S. & Preusser, F. (2022) Size–frequency distribution of shallow landslides in the Black Forest, Germany. *Earth Surface Processes and Landforms*, 47(1), 179–192. Available from: https://doi.org/10.1002/esp.5237